https://doi.org/10.1038/s44304-025-00101-7

Assessing extent of building damage following an earthquake: case study of the 2023 Turkey-Syria doublet

Guan Chen[1,2,3], Yong Liu[1] ✉, Zhangfeng Ma[2], Jiashu Yang[4], Michael Beer[5,6,7], Siau Chen Chian[3] ✉ & Shengji Wei[2,8,9] ✉

An earthquake doublet (M_w7.8 and M_w7.5) struck southeastern Turkey on February 6, 2023, causing widespread devastation. To evaluate seismic damage across 11 provinces, we analysed strong motion data, developed fragility functions and building damage state maps, validated by official reports and field surveys. Using five idealized structural models with varying fundamental periods, we estimated damage states for typical Turkish structures. The damage maps highlight how building period interacts with strong motion, providing valuable references for rapid assessment of building damage states and damaging potential of ground motions to various structures. Moreover, near-fault damage was significantly underestimated by seismic hazard maps based on empirical ground motion models, as observed ground motion intensities significantly exceeded predictions at R_{JB} less than 10 km. Additional phenomena associated with fault rupture, such as pulse-like ground velocities, surface fault displacements, and geohazards, further amplified damage. This study offers critical insights into near-fault seismic damage mechanisms and emphasizes the need for special tailored ground motion models for seismic hazard and risk assessment to enhance community resilience.

An earthquake doublet with moment magnitudes (M_w) of 7.8 and 7.5 occurred in Turkey on February 6, 2023. A M_w7.8 earthquake, with a depth of 10 km, struck southern Turkey near the Syrian border in Pazarcık, Kahramanmaraş Province, at 01:17:34 AM (UTC)[1]. This was followed 11 minutes later by a M_w6.7 aftershock[2]. The M_w7.8 event resulted from a strike-slip fault with geometrical parameters of approximately 190 km in length and 25 km in width. Its location, near the triple junction of the Anatolian, Arabian, and African plates, suggests that the East Anatolian Fault Zone or the Dead Sea Transform Fault Zone was the source. Later, a M_w7.5 earthquake, with a depth of 7.4 km, struck southern Turkey in Elbistan, Kahramanmaraş Province, at 10:24:48 AM, approximately 9 hours after the M_w7.8 event and about 95 km to the southwest[3]. The M_w7.5 event was also caused by a strike-slip fault, with dimensions of 120 km in length and 18 km in width, situated within the broader East Anatolian Fault Zone. The epicentres of these three events, along with the corresponding surface projections of the seismogenic fault, are depicted in Fig. 1.

The devastating earthquake doublet caused significant loss of life and property. The 11 southeastern provinces of Turkey, including Hatay, Adıyaman, Kahramanmaraş, Gaziantep, Osmaniye, Malatya, Kilis, Diyarbakır, Adana, Şanlıurfa, and Elazığ, which are home to approximately 15 million people, were declared disaster zones (Fig. 1A). The earthquake doublet claimed over 52,000 lives based on official damage report and caused an estimated $34.2 billion in direct physical damage[4]. In addition, according to Turkey's Ministry of Environment, Urbanization, and Climate Change[5], a total of 241,976 buildings were affected. Among these, 166,342 (about 68%) buildings sustained slight damage, 13,912 (about 6%) were moderately damaged, and 61,722 (about 26%) were heavy damaged, collapsed, or urgent demolished.

To better understand the characteristics of official damage data, we considered the relative and gross damage by province (Fig. 1B) and examined the correlation between mortality and Heavy-damaged, Collapsed, and urgently Demolished Buildings (HCDB) (Fig. 1C). We found

[1]State Key Laboratory of Water Resources Engineering and Management, Wuhan University, Wuhan, China. [2]Earth Observatory of Singapore, Nanyang Technological University, Singapore, Singapore. [3]Department of Civil and Environmental Engineering, National University of Singapore, Singapore, Singapore. [4]School of Civil Engineering, Xi'an University of Architecture and Technology, Xi'an, China. [5]Institute for Risk and Reliability, Leibniz Universität Hannover, Hannover, Germany. [6]Department of Civil and Environmental Engineering, University of Liverpool, Liverpool, UK. [7]International Joint Research Center for Resilient Infrastructure & International Joint Research Center for Engineering Reliability and Stochastic Mechanics, Tongji University, Shanghai, China. [8]Asian School of the Environment, Nanyang Technological University, Singapore, Singapore. [9]Key Laboratory of Deep Petroleum Intelligent Exploration and Development, Institute of Geology and Geophysics, Chinese Academy of Sciences, Beijing, China. ✉e-mail: liuy203@whu.edu.cn; sc.chian@nus.edu.sg; shjwei@gmail.com

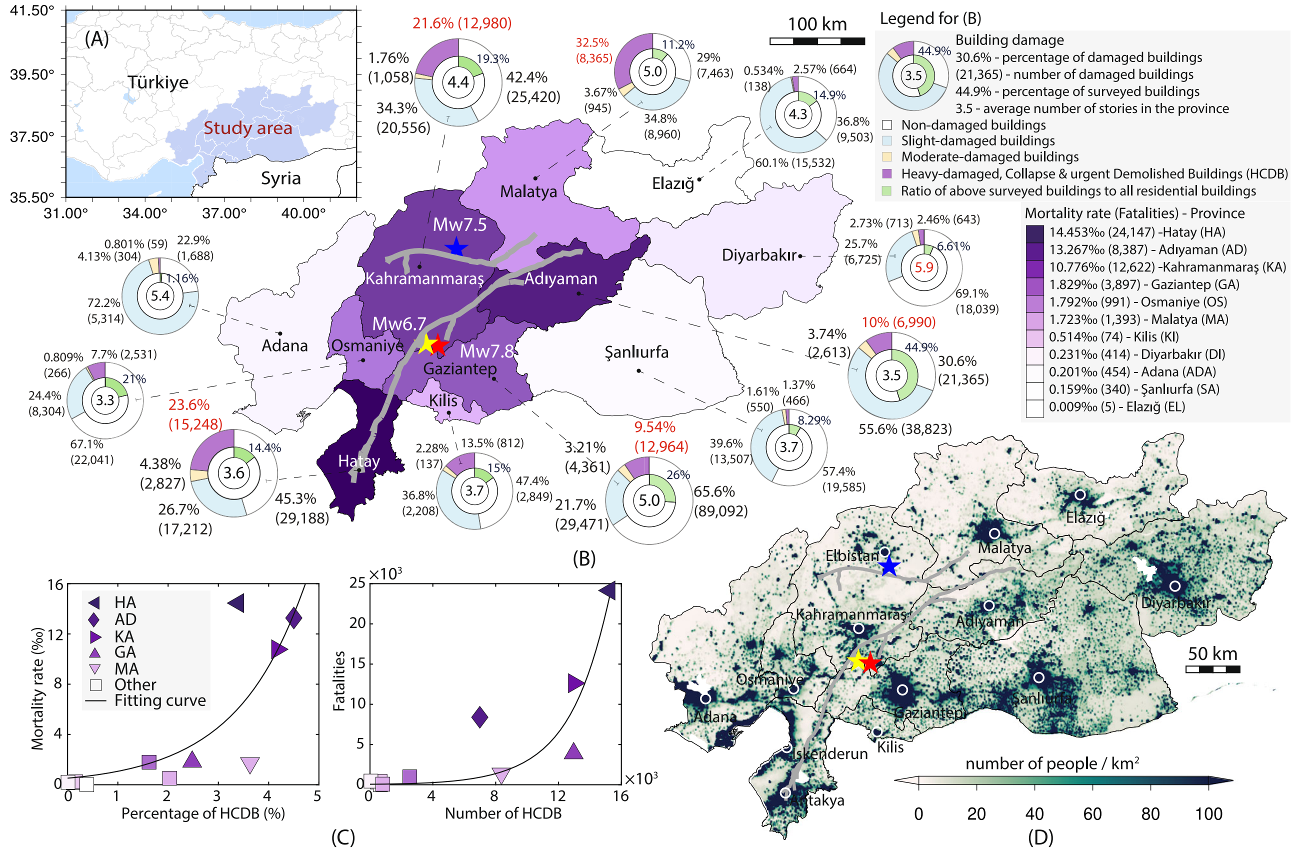

Fig. 1 | Mortality and building damage caused by the earthquake doublet. A Study area, including 11 provinces that were declared disaster zones by Ministry of Environment, Urbanization, and Climate Change of Turkey. **B** Mortality and building damage by province in the earthquake doublet, based on data from Turkey's Ministry of Environment, Urbanization, and Climate Change[5]. Four damage states, including non-damaged, slight-damaged, moderate-damaged, and Heavy-damaged, Collapse & urgent Demolished Building (HCDB) are classified. Percentage of surveyed buildings is the ratio of the surveyed building number (including four damage states) to all residential building number (data from Turkish Statistical Institute[46]), and the unsurveyed buildings are deemed as non-damaged. **C** Correlation between mortality and HCDB. Percentage of HCDB is the ratio of HCBD buildings to all residential buildings in the province, calculated by multiplying the percentage of damaged buildings by the percentage of buildings that were surveyed. We use the fitting curves to show the basic trend and identify outliers, rather than developing a fitting function for prediction. Sign color matches the colour of corresponding province in (**B**). **D** Population density of study area, based on data from Humanitarian Data Exchange[47]. Major cities are marked by white circle. Gray lines in (**B**, **D**) represent the surface projection of the seismogenic fault, based on data from Reitman et al.[50]. Red, blue, and yellow stars represent epicentre of the M_w7.8, M_w7.5, and M_w6.7 events, respectively, according to data from USGS[1–3].

that Hatay, Adıyaman, and Kahramanmaraş experienced the highest loss of life, both in terms of mortality rate and fatalities. The mortality rate in these three provinces exceeded 10‰ of the population and accounted for approximately 85% of the total fatalities. Compared to the regional consistency in relative and gross losses in mortality, the data for building damage revealed notable discrepancies. Specifically, Adıyaman, Kahramanmaraş, and Malatya ranked highest in relative HCDB damage, while Hatay, Kahramanmaraş, and Gaziantep had the highest gross HCDB damage. The correlation analysis further highlighted these differences. For instance, in the correlation analysis of relative damage, Hatay exhibited a high mortality rate but a relatively low percentage of HCDB in comparison with the fitting curve, whereas Malatya showed a high percentage of HCDB but a lower mortality rate. In the correlation analysis of gross damage, Adıyaman had a high fatalities but less HCDB damage compared to the fitting curve, while Gaziantep had significant HCDB damage but a relatively low fatalities. These differences in relative and gross building damage, as well as in their correlations with mortality, are influenced by various factors, such as shaking intensity, building types and quality, and population distribution. Hence, we provide additional data on population density (Fig. 1D), total population, and building-level distribution (Fig.S1) to support further discussion. For example, combining the damage data and population density, we could infer that the damage characteristics in Hatay Province may be influenced by the concentration of damage in Antakya, the largest city in the province, as higher population density in major cities likely contributed to a higher fatalities despite a relatively lower percentage of HCDB. Therefore, these data provide invaluable references for assessing the seismic damage and motivate us to further investigate the underlying causes of damage.

Extensive field investigations were conducted after the earthquake by various teams from Turkey, the United States, and Europe[5–8]. These investigations provided crucial insights into the factors contributing to the earthquake's consequences. The intensity of ground motion, inadequate seismic codes, poor construction quality, and geological and geotechnical hazards are usually highlighted as influencing factors for building damage[9,10]. For example, strong motion characteristics were examined by comparing records with empirical models[11,12], characterizing near-fault records[13–15], and assessing site effects on ground motion[16]. However, the spatial distribution of strong ground motions and their correlation with seismic damage remain largely unexplored. Structural engineers have identified excessive drift as the primary cause of damage to reinforced concrete (RC) buildings[9,17,18]. Geological and geotechnical hazards, particularly in near-fault regions[19], were also found to significantly affect buildings. For example, landslide-induced building damage was mapped using drone imagery in near-fault regions[20], while the effects of soil liquefaction on buildings were widely reported in the port city of Iskenderun, Hatay Province[21,22].

In addition to field investigations, remote sensing technologies such as Synthetic Aperture Radar (SAR) imagery[23] and optical imagery[24] played a crucial role in assessing the earthquake's consequences on a larger scale. However, validation is essential to ensure the accuracy of these remote sensing datasets, as different damage maps sometimes present inconsistencies[25].

In this study, strong motions and their impact on building are analyzed in detail. Specifically, we developed regional-scale maps for ground motion intensity by carefully reviewing and processing recorded strong motions. Based on nonlinear seismic analysis, fragility functions are developed to assess the damage states of buildings, where five types of structures are considered to represent the most common buildings observed in Turkish cities. The developed maps on ground motion intensities and building damage states were validated using official damage reports and field surveys. We identified the greater damage in the near-fault regions, and explored the underlying causes of the severe building damage and mortality in the earthquake doublet.

Results

Strong motion characteristics

Ground motion intensity measures (IMs), as parameters to describe the intensity of earthquake-induced shaking, are critical for seismic hazards and risk assessment. For example, the IMs in Performance-Based Earthquake Engineering (PBEE)[26], a popular framework for seismic hazard and risk analysis, are a critical component connecting the seismic hazard (e.g., earthquake magnitude) to the structural response (e.g., the maximum inter-story drift of a building)[27]. We therefore analysed the strong motion of the three largest events of M_w7.8, M_w7.5, and M_w6.7, including the statistical and spatial distribution of IMs, comparison with the empirical ground motion model (also called the ground motion prediction equation), and characterization of the near-fault records. The ground motions used in this study could be found in Table S7, with more details in Data availability.

We examined the statistical characteristics of 15 common ground motion IMs (Table S3), their correlation with engineering demand parameters (i.e., the maximum inter-story drift of buildings in this study), and their correlation with distance and site conditions, represented by the average shear wave velocity to 30 meters depth, V_{s30}. Statistical results show that spectral displacement, velocity, and acceleration generally follow a lognormal distribution, whereas the other IMs do not (Table S4). Nevertheless, Gaussian distribution fittings and the corresponding statistical parameters of the logarithmic IMs are also provided to facilitate a rapid assessment of strong motion intensity (Fig. S9). The correlation with the engineering demand parameter – obtained from nonlinear time-history analysis as detailed in Section S1 of the Supporting Information– indicates that although peak ground acceleration (PGA) and peak ground velocity (PGV) are among the simplest IMs, their correlation with engineering demand parameters is limited by the fundamental period of structures. Specifically, PGA generally correlates better with structures having shorter fundamental periods but performs poorly for structures with longer periods, whereas the opposite is true for PGV (Fig. S20). In contrast, the energy-frequency parameter (h), an IM defined in Chen et al.[28], shows the strongest correlation with the engineering demand parameter in structures with various fundamental periods (Fig. S20). Hence, we adopt the energy-frequency parameter to represent the intensity of strong motion and to connect to the building damage state. Additionally, we found that the ground motion IMs, including PGA, PGV, and the energy-frequency parameter, are generally more sensitive to distance compared to V_{s30} (Fig. S19 and Table S5). However, site conditions are detected as one of the key influencing factors for ground motion intensity[16,29], raising concerns about the applicability of V_{s30} to reflect the effects of site characteristics on ground motion accurately.

We tested the spatial distribution of ground motion intensity for the M_w7.8, M_w7.5, and M_w6.7 events separately (Fig. S13), where PGA, PGV, and the energy-frequency parameter are used. We also provided maps based on the maximum values recorded at monitoring stations, irrespective of the seismic source, to better reflect the shaking intensity map caused by the earthquake doublet and aftershock (Fig. 2A for energy-frequency parameter and Fig. S13 for PGA and PGV). We found that ground motion caused by the aftershock has minimal impact on the maximum-value-based IM map and that ground motion intensity is much stronger along the seismogenic fault. Furthermore, we compared our developed maps with the empirical ground motion model (Fig. S18), and found that the IM spatial distribution based on recorded strong motions is irregular, with several extremely high spots highlighted in the green rectangles in Fig. 2A. Although these irregular features, partially due to the lack of records, prevent our model from perfectly capturing the ground motion characteristics, it more effectively highlights the unique and actual spatial patterns of ground motion intensity in near-fault regions – an aspect that is often overlooked by empirical ground motion models (Figs. S17 and S18). For example, the highlighted rectangle areas basically agree with the supershear rupture segments identified in Abdelmeguid et al.[30]. In addition, we found different spatial features among the IMs by graphic comparison. Specifically, compared to PGV, PGA exhibits different locations for its maximum values, and attenuates more rapidly with increasing distance (Fig. S13), which aligns with the consensus that high-frequency components attenuate faster. The maximum-value-normalized map (Fig. S14) indicates that the h shares a similar peak location with PGV, but attenuates much slower than PGV with effectively highlights ground motion intensities in near-fault regions. These characteristics may explain the divergence in their correlation analysis with engineering demand parameters (Fig. S20).

To gain a deeper understanding of the shaking intensity generated by the earthquake doublet, we compared ground motion IMs—including PGV, PGA, and pseudo-spectral acceleration—from the M_w7.8, M_w7.5, and M_w6.7 events with the AB10 model[31]. This is an empirical ground motion model for Europe, the Mediterranean region, and the Middle East, and validated for reliable performance in this region compared to other models (Fig. S16). We found that the empirical ground motion model generally underestimates ground motion intensity at R_{JB} distances less than 100 km, particularly for R_{JB} less than 10 km, while overestimating the intensity at R_{JB} greater than 100 km. R_{JB} is the Joyner-Boore distance, which measures the shortest distance from a site to the surface projection of seismogenic fault[32]. For instance, in the M_w7.8 event, observed PGVs at R_{JB} less than 10 km exceed the average values predicted by the model, with some data points even falling outside the range of one standard deviation (Fig. 2B). We also observed a similar trend in the PGA comparison (Fig. 2C). All recorded PGAs are greater than predicted mean values at R_{JB} less than 10 km, except for PGA of the '0213' station, which is below the average value. However, upon review the time-history curve, we found that this station failed to record the entire waveform (Fig. 4B, C). Hence, the shaking intensity in this earthquake doublet is much stronger than predicted value from the empirical model, particularly in near-fault regions (e.g., R_{JB} less than 10 km).

We specifically analyzed near-fault waveforms due to their significantly stronger intensity and the pulse-like ground motions, which are characterized by long-period, high-amplitude pulse components in velocity and widely recognized for amplifying seismic demands in engineering practices[33–35]. We identified all near-fault pulse-like records in M_w7.8, M_w7.5, and M_w6.7 events and provided the corresponding seismic velocity waveforms (Fig. S5 and S6). We found that the IMs of near-fault pulse-like ground motions are generally stronger than the values predicted by the empirical ground motion model (Figs. 2B, C) and S17), indicating that near-fault characteristics are not well captured in empirical models. In addition, we observed that the identified near-fault pulse-like ground motions in M_w7.8 and M_w6.7 events are generally along the seismogenic fault (Figs. S5 and S6), which indicates that the pulse generation in these events is closely related to forward directivity effects[36]. Moreover, we observed that pulses caused by forward directivity effects typically appear in both horizontal components and, in some cases, even in the vertical component. In contrast, pulses generated by other factors (e.g., site effects) are orientation-sensitive and usually occur randomly in a single component, such as the

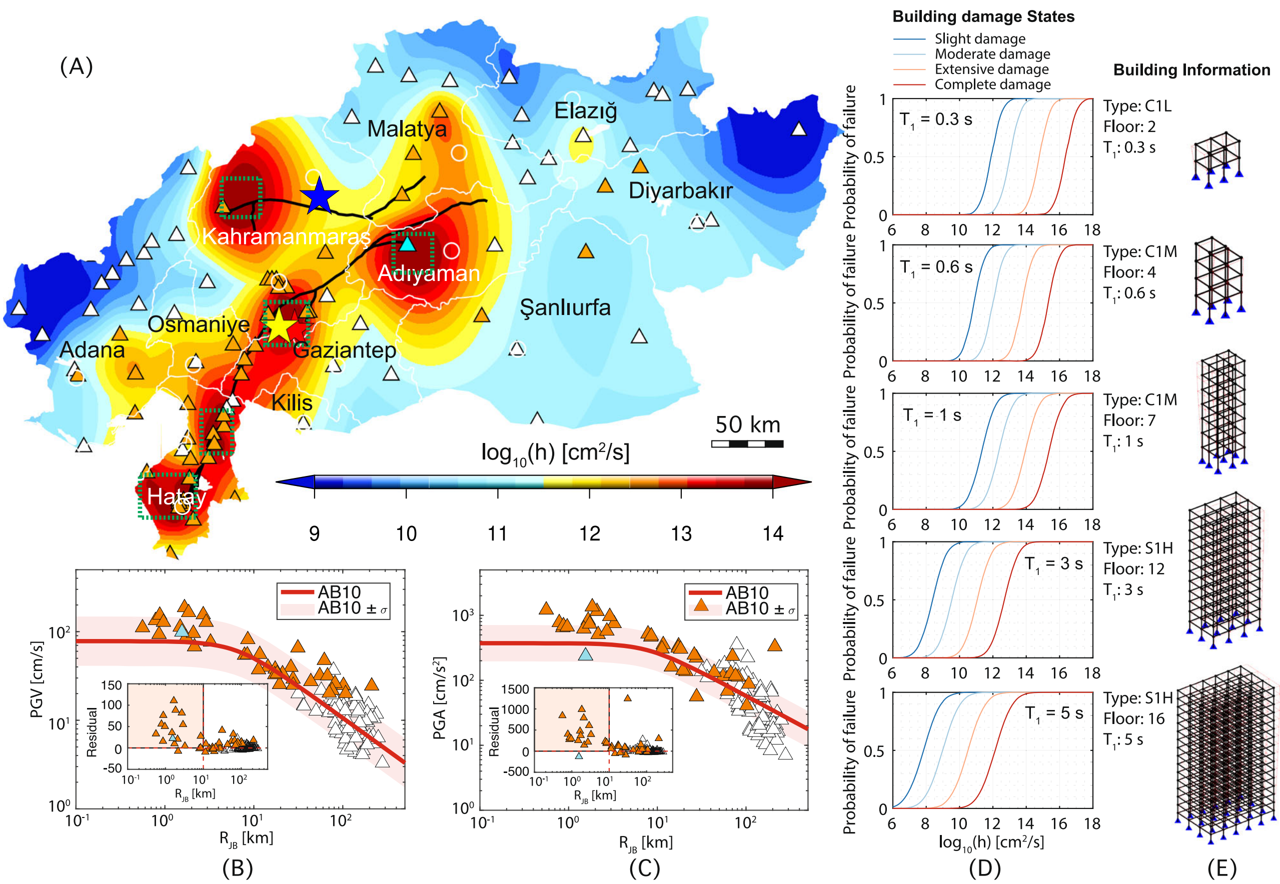

Fig. 2 | Ground motion characteristics and fragility functions for various buildings. **A** Spatial distribution of shaking intensity by the earthquake doublet, represented by the energy-frequency parameter (h) as defined in Chen et al.[28]. Shaking intensity of individual event is provided in Fig. S13. Black line represents the surface projection of the seismogenic fault[50]. Triangles indicate the selected monitoring stations from AFAD (Table S7), where white and orange color represent ordinary- and pulse-like records, respectively. Cyan triangle marks the station `0213'. Red, blue, and yellow stars represent the epicenters of the M_w7.8, M_w7.5, and M_w6.7 earthquakes, respectively. Dashed green rectangles highlight the areas with great stronger ground-motion intensity. White circle is the marked major cities in Fig. 1(**D**). (**B**, **C**) compared the recorded PGV and PGA in M_w7.8 event with predicted values from the ground motion prediction equation, AB10 model[31], respectively. R_{JB} represents the closest distance from a site to the surface projection of seismogenic fault. Residual is the difference between recorded and predicted value, which highlights that the empirical model significantly underestimates the ground motion intensities as $R_{JB} < 10$ km. **D** Fragility functions for buildings with fundamental periods (T_1) of 0.3 s, 0.6 s, 1 s, 3 s, and 5 s. **E** Building information, with building type classified according to FEMA Hazus 5.1[37]. More details about the building modeling are provided in Tables S1 and S2, along with Fig. S2 and S3 in Section S1.

pulse-like records in M_w7.5 event (Fig. S5) and the far-fault pulse-like records in M_w7.8 event (Fig. S6C).

Building damage assessment

Local building information, such as structural type, height, and fundamental period, can significantly enhance the assessment of building damage. However, only the distribution of building floors at the provincial scale was available (Fig. S1A), and detailed on-site building data were not accessible. Therefore, rather than developing a site-specific building damage model, we adopted five representative frame structure types, using their fundamental periods as key indices to represent the most common buildings and infrastructure in Turkish cities[10,18]. Corresponding fragility functions were developed to describe the damage states of various building types under seismic excitations (Fig. 2D, E). Thus, our work effectively provides the damaging potential of ground motions in this earthquake sequence to various structures. Moreover, once the building type at a given site is identified, the expected damage can be assessed using the associated fragility function effectively and efficiently.

To develop fragility function, we first employed time-history analysis to capture the nonlinear seismic response of various buildings subjected to each recorded ground motion, where five types of frame structures with fundamental periods ranging from 0.3 s to 5 s are adopted (Fig. 2E). Next, regression analysis was applied to connect ground motion intensity (represented by the energy-frequency parameter, $\log_{10}(h)$, in this study) with building response (measured as the maximum inter-story drift) (Fig. S21A). We employ maximum inter-storey drift to assess building damage states, as it is a critical criterion for evaluating structural performance and has been consistently emphasized in field investigations[7,18]. Finally, we developed fragility functions by quantifying the uncertainties in the residuals, where the damage state threshold values defined in FEMA Hazus 5.1 (Table S6) is employed[37]. Of note, FEMA threshold values may not perfectly reflect building damage states in Turkey due to regional differences in construction quality and building types. However, given the lack of region-specific drift-based thresholds in Turkish seismic codes (including TEC 2007[38] and TBEC 2018[39]) and the practical challenges of developing a localized damage model, we adopted the FEMA Hazus thresholds as a reasonable and adaptable reference for assessing building damage states. Additional methodological details about the fragility functions are provided in Sections S1 and S3 of the Supporting Information.

Combined with the fragility functions and the spatial distribution of the energy-frequency parameter (h) in Fig. 2A, we could easily assess the risk for various building types in different regions caused by the earthquake doublet. For example, when $\log_{10}(h)$ is 13, buildings with fundamental periods of 0.3 s, 0.6 s, 1 s, 3 s, and 5 s have probabilities of approximately 0%, 5%, 5%, 100%, and 100% of being extensive damaged, or 0%, 0%, 0%, 70%, and 85% of being completely damaged, respectively.

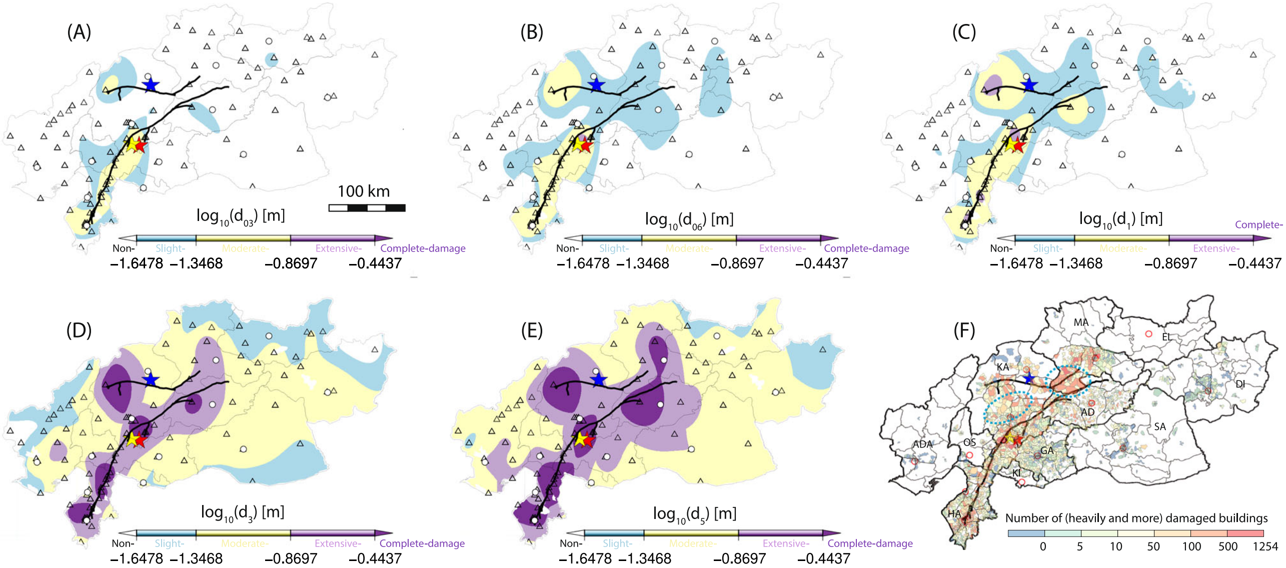

Fig. 3 | Building damage characteristics. Spatial distribution of damage states for building with fundamental periods of (**A**) 0.3 s, (**B**) 0.6 s, (**C**) 1 s, (**D**) 3 s, and (**E**) 5 s. Four states, non-, slight-, moderate-, extensive, and complete-damage, are classified based on the thresholds of maximum inter-storey drift (*d*) defined in FEMA Hazus 5.1 (Table S6), where *d* is calculated by nonlinear time history analysis. **F** Number of heavy-damaged, collapse and urgent demolished buildings assessed by the Ministry of Environment, Urbanization, and Climate Change. This data is aggregated at the neighbourhood (Mahalle) level from Shelter Sector Türkiye, Global Shelter Cluster[51], where the dashed ellipse indicates the areas that are not well captured by our model. Red, blue, and yellow stars represent the event epicenters for M_w7.8, M_w7.5, and M_w6.7, respectively. Triangle represents the monitoring stations. Circle indicates the major cities followed in Fig. 1D. Black line represents the surface projection of the seismogenic fault[50].

Based on the maximum inter-storey drift of buildings, we further analysed the spatial distributions of various damage states in buildings (Fig. 3A–E) and found that they basically align with the spatial patterns of ground motion intensity (Fig. 2A). Regions experiencing stronger ground motion tend to exhibit more severe building damage. For instance, the green rectangle areas in Fig. 2A, which highlight zones of the strongest ground motion intensity in the earthquake doublet, experienced the most severe building damage. Our results also basically match the HCDB in official data, such as the widespread damaged buildings in the Hatay, Adıyaman, and Kahramanmaraş provinces (Fig. 1B, C). We also found that our damage model (Fig. 3E) encompasses the majority of observed damage (Fig. 3F). Therefore, our model adequate for representing overall building damage. Of note, while we adopt building damage state map in Fig. 3E for comparison, it does not mean all damage in Fig. 3F is attributable to structures with fundamental periods near 5 s; losses also arise from buildings with different dynamic characteristics, construction quality, and structural types. For example, masonry buildings may experience more severe damage than frame structures under the same seismic conditions.

We also found that high-rise buildings tend to suffer more severe damage than low-rise buildings at the same site. Similar results can also be observed in official damage data. For example, the Diyarbakır and Adana provinces have much higher mortality rates compared to the Elazig province, despite all three being far from the epicenter and the seismogenic fault and experiencing similar ground motion intensities (Figs. 2A, 3F). This discrepancy may be attributed to the prevalence of high-rise buildings in the Diyarbakır and Adana provinces. Specifically, Diyarbakır has the highest average building height at 5.9 floors, with 49% of its buildings exceeding six floors, while Adana has the second-highest average building height, with 33.3% of its buildings exceeding six floors. In contrast, the average building height in the Elazig province is 4.3 floors (Figure S1A).

However, some affected zones are not fully captured by our damage model, as highlighted by the dashed ellipse in Fig. 3F. This may be due to the limited number of monitoring stations and the omission of cumulative effects. For example, no stations were present in the southern Malatya Province during the M_w7.5 event (Figure S7), and cumulative effects were not considered, despite the close proximity of the M_w7.8 and M_w7.5 fault. A similar situation is also observed in Kahramanmaraş, as indicated by the dashed ellipse in the southern region, which experienced more severe damage than the northern region with seismogenic fault as dividing line. Further details about the discrepancies are provided in the Discussion section.

Discussion

Various maps are developed in this study to illustrate the spatial distribution of ground motion intensity and the damage states of various buildings to support the assessment of seismic damage caused by the earthquake doublet. However, by comparing the ground motion intensity distribution (Fig. 2A) with the observed building damage data (Fig. 3F), we found that the intensity map not perfectly captures the actual damage patterns. For example, the intensity map effectively highlights the extensive damage in Hatay province; however, it only partially captures the extent of damage in other provinces, such as Adıyaman, Kahramanmaraş and Malatya. Herein, we use ground motion intensity map for comparison instead of a site-specific building damage model, owing to the unavailability of detailed site-specific structural inventory required for the development of such models. The discrepancy between our results and the observed data can be attributed to several factors, including variations in ground motion, building types and quality, population density, surface displacement, and geological and site conditions. To address this, we examined how these factors contribute to population and building losses, why our analysis only partially reflects earthquake-induced damage, and how seismic damage assessments can be improved by integrating multi-source data.

Ground shaking is one of the most significant causes of extensive losses in earthquakes. We carefully reviewed the strong motions in the earthquake sequences and selected the monitoring stations in the study area where the seismic waveforms were fully recorded (Fig. S7 and Table S7). Some selected strong motions from the M_w7.8 earthquake are shown in Fig. 4A. The corresponding velocity and acceleration waveforms, along with the p-wave arrival time, R_{JB}, epicentral distance, PGV, and PGA, are presented in Fig. 4B. Stations that failed to capture the complete seismogram were excluded, as incomplete data could lead to inaccurate spatial distributions of ground motion intensity and potentially incorrect assessments of seismic damage

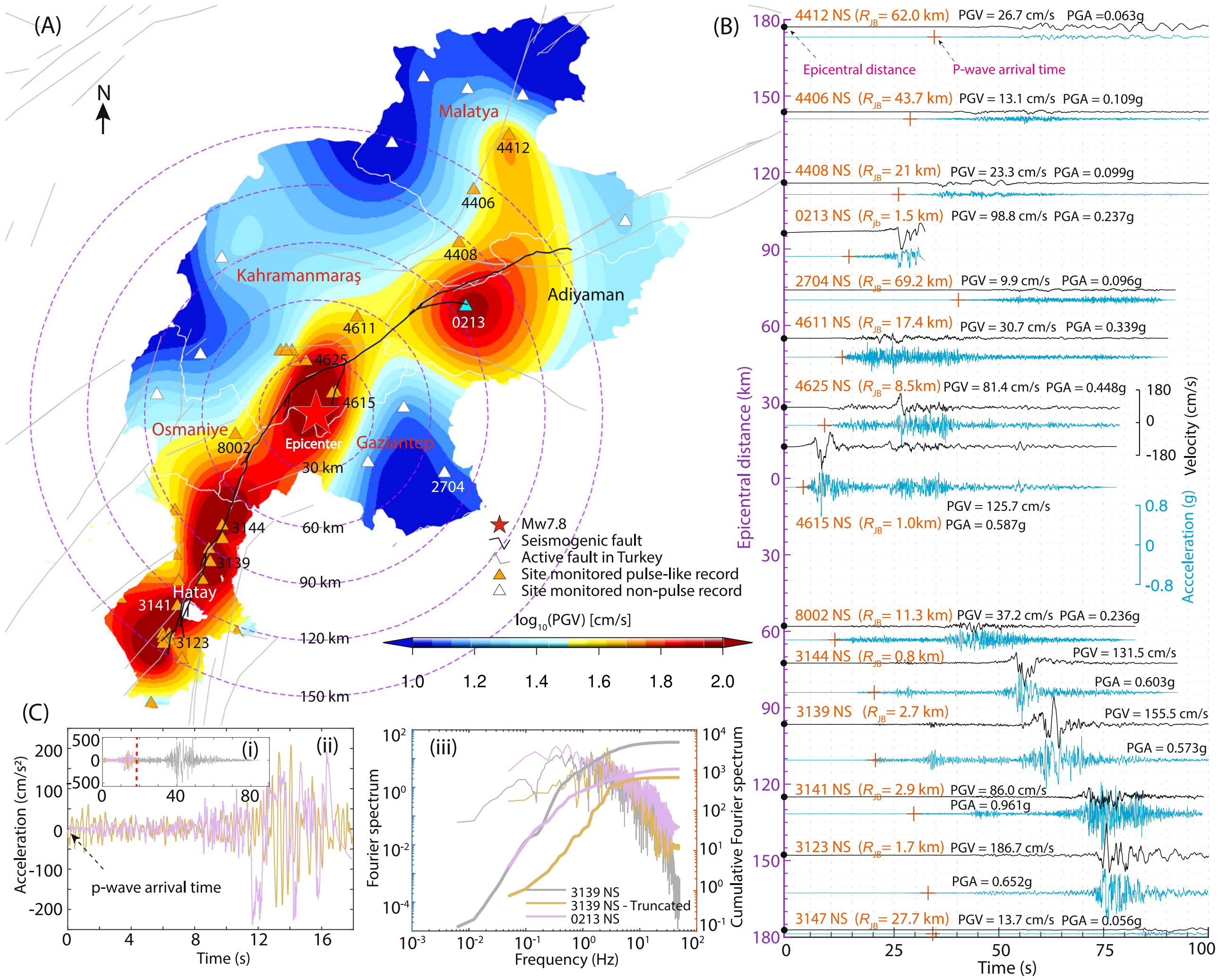

Fig. 4 | Strong-motion records in M$_w$7.8 earthquake. A Spatial distribution of selected monitoring stations. **B** Velocity and acceleration waveforms, where starting point (i.e., time is 0) is the event occurrence time. Black dot corresponds to the epicentral distance of the station, and the '+' indicates the p-wave arrival time. **C** Time- and Frequency-domain comparison between '0213' and '3139' stations, where the Fourier spectrum and cumulative Fourier spectra are provided. Active fault in Turkey is from Emre et al.[52]. More waveforms of the selected monitoring stations could be found in Fig. S8.

(Figs. S11 and S12). Therefore, the limited seismic records are an important reason why this study can only partially reflect the actual losses.

We observe that no complete waveforms were recorded in Adıyaman province during the M$_w$7.8 event (Fig. 4). This can be attributed to several factors, including the quality and quantity of strong motion monitoring equipment[40], as well as broader issues such as funding support, public awareness of seismic hazards, and the province's economic conditions. However, since Adıyaman province is reported to have the second-highest mortality rate in the official data (Fig. 1C), we can infer that the intensity of ground motion in this province may be similar to that in Hatay and significantly higher than suggested by the shaking map in Fig. 2A. We have several pieces of evidence to support this inference. On one hand, Adıyaman's position relative to the seismogenic fault and the epicenter is similar to that of Hatay (Fig. 4A). While station '0213' did not capture the full waveform, the partial signal indicates that its intensity may be comparable to that recorded at station '3139' considering their similarity in epicentral distances and R_{JB} (Fig. 4B). To further validate this inference, a comprehensive waveform comparison on both time- and frequency-domain are conducted between '0213' and '3139' stations, as shown in Figs. 4C and S15. It indicates that the truncated '3139' waveform shows strong similarity in waveform characteristics of '0213' in time domain, like PGA and amplitude envelope (Fig. 4(C-i and ii)). The cumulative Fourier energy of '0213' also closely resembles that of the truncated '3139' waveform, with energy concentrated predominantly in the lower-frequency range (Fig. 4(C-iii)). Therefore, the recorded waveform at '0213' station successfully represents the early characteristics of ground motion but lacks the high-energy components present in the later part of the signal. Given the strong time- and frequency-domain similarity between the truncated '3139' and the available portion of '0213', as well as the similar R_{JB} and epicentral distance, we infer that the missing portion of '0213' may have continued similarly to that of '3139'. Therefore, the energy-frequency parameter in Fig. 2A derived from the partially available '0213' station are likely to underestimate the real ground motion intensity. On the other hand, the empirical ground motion model (Fig. S18) and simulation results of 3D dynamic rupture modelling[41] also support this inference. While both the empirical model and numerical simulations face challenges in fully capturing the characteristics of near-fault ground motion, they can still provide valuable insights. Therefore, our analysis underestimated the seismic damage in Adıyaman province, largely due to the lack of strong motion data.

In contrast, we have sufficient recorded strong motions in Hatay province to support our model in assessing the seismic damage objectively. Next, we discuss why Hatay province, located approximately 150 km from the epicenter, experienced the most severe damage. The obvious factors are the extremely high shaking intensity in near-fault regions (Fig. 2A–C) and the pulse-like records observed in the province, such as '4615,' '3144,' and '3139' (Figs. 4B and S6). These pulse-like motions are also known to significantly increase seismic demands[33,34]. Furthermore, we explored the underlying reason for the stronger intensity and pulse-like characteristics of ground motions from the seismological perspective, and suggested that it may be due to the supershear rupture of the fault segment in Hatay province[30]. A supershear rupture could result in the superposition of seismic waveforms, amplifying the intensity of ground motion and generating pulse-like records due to Doppler effects (also called forward directivity effects in engineering)[36]. For example, the areas with the strongest ground-motion intensity in Hatay province, which is highlighted by rectangle in Fig. 2A, align with the supershear rupture segments identified in Abdelmeguid et al.[30]. The distribution of pulse-like records also has a clear orientation along the fault rupture direction (Fig. 4A). In addition to ground shaking, fault displacement (Fig. S22) and geohazards, such as landslides[20] and soil liquefaction[22], further exacerbate the damage in Hatay province.

Building types and construction quality are other significant factors contributing to the extensive damage in the earthquake doublet. Our results on building damage assessment (Fig. 3) highlight that high-rise buildings tend to suffer much more severe damage than low-rise buildings, and explain how this affects seismic damage in different provinces. While field surveys revealed that construction quality is another critical cause of the severe building damage[9,10,18], we use Adıyaman province as an example to explain how construction quality affects the damage characteristics. Compared to Hatay and Kahramanmaraş provinces, where major cities were affected by the earthquake doublet, the seismogenic fault is far from the major city of Adıyaman province and located in its northern region, which has much lower population density (Fig. 1D). Lower population density generally correlates with lower building heights, which typically results in less building damage, as analyzed in our results (Figs. 2 and 3). However, Adıyaman province exhibits the highest percentage of HCDB damage among these three provinces, with mortality rates similar to Hatay and Kahramanmaraş provinces (Fig. 1C). This discrepancy may be attributed to the widespread use of masonry buildings in Adıyaman's rural areas, which were severely damaged during the earthquake[42].

The discrepancies between our results and observations also arise from limitations in our building models, analysis resolution, and methodologies. In this study, we use concrete and steel frame structures to represent the majority of building types in cities, following general seismic design codes. However, these building types do not fully capture the diversity of structures, particularly in rural areas. Additionally, the cumulative effects of multiple seismic events on structural damage are not considered in this study due to the limited number of stations that recorded waveforms from all three events, as well as the significant spatial separation (approximately 95 km) between the two mainshocks, which makes the effects of subsequent seismic excitations on building damage insignificant, except the southern Malatya and Kahramanmaraş provinces, which are highlighted by the dashed ellipses in Fig. 3F. Lastly, since some data are collected at the provincial scale (e.g., official damage data and building distribution data), the severity of damage may be underestimated in areas where the population is concentrated in regions experiencing high-intensity ground shaking.

Although our result, like other single-source data, is limited in accurately assessing the seismic damage, we can integrate multi-source data, including ground motion, building height and quality, field surveys, and population density, to improve the accuracy of seismic damage evaluations. We take Malatya province as an example to demonstrate how integrating multi-source data can enhance it. First, our model in Fig. 2A likely underestimates the ground motion intensity in Malatya province, as no records are available near the seismogenic fault of the M_w7.5 earthquake in this region (Fig. S7). However, based on the waveform recorded at station '4612', located on the opposite side of the seismogenic fault during the M_w7.5 event, which shows extremely high ground motion intensity (Fig. S8), we infer that the ground motion intensity near the seismogenic fault in Malatya province should be similar to the region near monitoring station '4612'. Moreover, southern Malatya Province is the only region in close proximity to the seismogenic faults of both major earthquakes, and the cumulative effects likely amplified the extent of the damage in this area. The concentrated building damage observed in this region (Fig. 3F) could validate our inference about the ground motion intensity. Second, the building height and quality likely exacerbate the damage. The average building height in Malatya province is 5.0 floors, the third highest in the study area (Fig. S1A); and poor building quality in Malatya province was also highlighted in field investigations[43,44]. Finally, the population density near the seismogenic fault of the M_w7.5 event in Malatya province was much lower (Fig. 1D), which could contribute to the lower mortality rate. We therefore infer that the damage characteristics of Malatya province are likely to show high levels of building damage but relatively low mortality, a pattern that aligns with the official damage data presented in Fig. 1C.

In summary, to improve the assessment of seismic damage caused by the 2023 Turkey-Syria earthquake doublet, we developed ground motion intensity maps based on recorded data through careful review and comprehensive analysis, along with fragility functions and damage state maps for structures with varying fundamental periods. Moreover, the strategy of integrating multi-source data is practical and effective for advancing seismic damage evaluation. Results indicate that empirical ground motion models significantly underestimate shaking intensities in near-fault regions, particularly as $R_{JB} < 10$ km. Buildings in this area also suffer most severe damage, which is basically revealed by our damage model. Moreover, the fault rupture characteristic plays a crucial role in seismic damage pattern. For example, in the M_w7.8 event, the areas with the highest ground motion intensities align well with supershear rupture segments. The pulse-like ground motions, which are validated to increase seismic demands, are also closely related to the rupture direction.

Based on our observations and analysis of this earthquake, we suggest that (1) development of specialized models for near-fault ground motion is urgently needed. Empirical models tend to significantly underestimate ground motion intensities in near-fault regions, as demonstrated in this earthquake. Given the extreme damage observed and the wealth of near-fault recordings from this earthquake doublet, there is a valuable opportunity to develop and calibrate ground motion models tailored for near-fault conditions. (2) Improvement of seismic design codes is necessary by more precisely accounting for building classification. Building damage varies significantly depending on structural type, construction quality, and dynamic properties such as the fundamental period (closely related to building height). Our analysis highlights the substantial variability in damage outcomes due to these factors. For more refined seismic design, codes should incorporate these considerations more explicitly. Furthermore, maximum inter-story drift is a practical parameter for building damage assessment, and it shall work better if it were supported by detailed guidelines that account for different damage states across various building types and conditions. (3) Integration of seismological principles into seismic hazard and risk assessments is essential. Fault rupture characteristics, such as rupture direction and speed, have a significant impact on ground motion. Secondary geohazards, such as landslides and surface fault displacement, are also closely related to fault rupture. We, as a community focused on earthquake disaster, usually pay more attention on structural response under seismic excitations and less considering the seismological principles. However, we must place greater emphasis on seismology and geophysics to better understand and predict earthquake impacts.

The development presented in this study contributes to the advancement of the United Nations Sustainable Development Goals (SDGs), particularly SDG 9 and SDG 11. By enhancing the understanding of strong-motion characteristics and near-fault ground shaking, our findings support the design of resilient infrastructure and the implementation of improved seismic hazard mitigation strategies, aligning with SDG 9: "Build resilient infrastructure, promote inclusive and sustainable industrialization, and foster innovation." Furthermore, by providing insights into earthquake impacts on urban areas, this research aids in the development of safer and more sustainable cities, contributing directly to SDG 11: "Make cities and human settlements inclusive, safe, resilient, and sustainable." The improved assessment of seismic risks can inform urban planning, building codes, and disaster preparedness strategies, ultimately enhancing the resilience of communities to future earthquakes.

Methods

This study employed a rigorous and systematic approach to assess damage in the catastrophic 2023 Turkey-Syria earthquake sequence by integrating ground motion analysis, nonlinear time-history simulations, and building fragility function development. We initially collected seismic records for the three major events in the earthquake sequence: M_w7.8, M_w7.5, and M_w6.7. The basic information about the earthquakes, including magnitude, location, and depth of the earthquakes, and occurrence time, was based on the data from USGS[1–3]. The recorded waveforms were obtained from the Turkey Ministry of Interior Disaster and Emergency Management Presidency (AFAD)[45]. The spatial distribution of monitoring stations, along with the epicentral distance and V_{s30} distribution for the three earthquakes, is shown in Fig. S4. This study focuses on the 11 provinces officially reported to have experienced earthquake-induced damage (Fig. 1A). The selected monitoring stations in the study area that were recorded the entire waveform are represented by triangles in Fig. S7 and listed in the Table S7 in the Supporting Information. To ensure the reliability of the ground motion intensity map, stations that partially recorded or failed to capture the seismic waveforms must be excluded from the analysis. The official damage data in the study area[5], residential building characteristics[46], and population density[47], were also collected.

We conducted a series of analyses to evaluate ground motion characteristics. Distribution fitting and corresponding statistical parameters (mean and standard deviation) for 15 commonly used ground motion IMs (Table S3) are provided in Fig. S9. Additionally, we analyzed the spatial distribution of ground motion IMs. The unsampled locations are estimated by ordinary Kriging method due to its advantages on unbiased estimates, where the stable model is employed to fitting the variogram and represent the spatial correlation[48]. However, due to the unavoidable errors of the interpolated value, the monitoring stations are also marked in figures for distinguishing recorded and Kriging estimated value. More details about the Kriging method and the effects of semi-variograms on interpolation results (Figure S10) could be found in section S2.5.1 of Supporting Information. To identify near-fault pulse-like ground motions in the three major events, we applied a generalized continuous wavelet transform method proposed by Chen et al.[49] (Figs. S5, S6). This method overcome the limitation of classical continuous wavelet method for requiring a wavelet basis, and provide a more flexible frame to detect various pulse types. Using the empirical AB10 model[31], we compared the observed ground motion IMs with empirical values (Fig. S17) and developed empirical maps for PGA and PGV (Figure S18). The reliability of AB10 model is verified by comparing with other models (Fig. S16). Furthermore, correlation analyses among IMs, distance, V_{s30}, and engineering demand parameters were performed (Figs. S19, S20, and Table S5).

The fragility functions were developed to describe the probability of building damage states in the earthquake doublet. The finite element method was used to capture the nonlinear seismic response of buildings under recorded strong motions. Details regarding the numerical modeling, constitutive model, geometric and mechanical parameters of the structures, are provided in Section S1. More details about the development of fragility functions are in Section S3.

Data availability

Ground motions for the events M_w7.8, M_w7.5, and M_w6.7 are from AFAD, Turkey (https://tadas.afad.gov.tr/list-event). Specifically, this study utilizes data from 175 monitoring stations, as listed in Table S7 of the Supporting Information. The set of stations used for each event may vary, as some stations failed or only partially recorded seismic waveforms; the stations included for each event are shown in Fig. S7. Velocity waveforms from provinces that experienced high ground motion intensity are presented in Fig. S8. The acceleration data, in ASCII format, were originally downloaded from the AFAD website. Notably, M_w7.8, M_w7.5, and M_w6.7 in USGS correspond to M_w7.7, M_w7.6, and M_w6.6 in AFAD, respectively. Other involved data are cited in the text.

Received: 11 March 2025; Accepted: 5 June 2025;
Published online: 26 June 2025

References

1. USGS Earthquake Hazards Program. M 7.8 - Pazarcik earthquake, Kahramanmaras earthquake sequence https://earthquake.usgs.gov/earthquakes/eventpage/us6000jllz/executive (2023).
2. USGS Earthquake Hazards Program. M 6.7 - 14 km E of Nurda??, Turkey https://earthquake.usgs.gov/earthquakes/eventpage/us6000jlm1/executive (2023).
3. USGS Earthquake Hazards Program. M 7.5 - Elbistan earthquake, Kahramanmaras earthquake sequence https://earthquake.usgs.gov/earthquakes/eventpage/us6000jlqa/executive (2023).
4. World Bank Group. Earthquake Damage in Türkiye Estimated to Exceed $34 billion: World Bank Disaster Assessment Report https://www.worldbank.org/en/news/press-release/2023/02/27/earthquake-damage-in-turkiye-estimated-to-exceed-34-billion-world-bank-disaster-assessment-report (2023).
5. Cetin, K. O., Ilgac, M., Can, G. & Cakır, E. Preliminary reconnaissance report on February 6, 2023 Kahramanmaraş-Pazarcık (Mw=7.7) and Elbistan (Mw=7.6) Earthquakes. Tech. Rep., Middle East Technical Univeristy: Earthquake Engineering Research Center https://eerc.metu.edu.tr/en/announcement/metu-eerc-preliminary-report-pazarcik-kahramanmaras-mw-77-and-elbistan-kahramanmaras-mw (2024).
6. Cetin, K. O. et al. February 6, 2023 Turkiye Earthquakes: Report on Geoscience and Engineering Impacts. Tech. Rep. GEER Association Report 082, Earthquake Engineering Research Institute, LFE Program https://learningfromearthquakes.org/resources/february-6-2023-t-rkiye-earthquakes-report-on-geoscience-and-engineering-impacts/ (2023).
7. Aktas, Y. et al. The Turkiye earthquake sequence of February 2023: A longitudinal study report by EEFIT. Tech. Rep., EEFIT https://discovery.ucl.ac.uk/id/eprint/10186995/ (2024).
8. Dilsiz, A. et al. StEER: 2023 Mw 7.8 Kahramanmaras, Türkiye Earthquake Sequence Preliminary Virtual Reconnaissance Report (PVRR). Tech. Rep. (2023).
9. Altunsu, E. et al. Investigating the structural damage in Hatay province after Kahramanmaraş-Türkiye earthquake sequences. *Eng. Fail. Anal.* **157**, 107857 (2024).
10. Ozturk, M., Arslan, M. H. & Korkmaz, H. H. Effect on RC buildings of 6 February 2023 Turkey earthquake doublets and new doctrines for seismic design. *Eng. Fail. Anal.* **153**, 107521 (2023).
11. Buckreis, T. E. et al. Engineering attributes of ground motions from February 2023 Türkiye earthquake sequence. *Earthquake Spectra* 87552930241259024 (2024).
12. Altindal, A. & Askan, A. Traditional seismic hazard analyses underestimate hazard levels when compared to observations from the 2023 Kahramanmaras earthquakes. *Commun. Earth Environ.* **5**, 14 (2024).
13. Baltzopoulos, G. et al. Near-source ground motion in the M7. 8 Gaziantep (Turkey) earthquake. *Earthq. Eng. Struct. Dyn.* **52**, 3903–3912 (2023).
14. Kazaz, İ., Bilge, İ. H. & Gürbüz, M. Near-fault ground motion characteristics and its effects on a collapsed reinforced concrete structure in Hatay during the February 6, 2023 M_w7. 8 Kahramanmaraş earthquake. *Eng. Struct.* **298**, 117067 (2024).
15. Chen, G. Report on pulse-like ground motions in the Feb 2023 Turkey earthquakes. *Preprint* https://doi.org/10.13140/RG.2.2.31375.25767 (2023).
16. Demir, A. et al. Destructive impact of successive high magnitude earthquakes occurred in Türkiye's Kahramanmaraş on February 6, 2023. *Bull. Earthq. Eng* **23**, 1–27 (2024).

17. Vuran, E. et al. Damage observations of RC buildings from 2023 Kahramanmaraş earthquake sequence and discussion on the seismic code regulations. *Bull. Earthq. Eng.* **23**, 1–30 (2024).
18. Pujol, S. et al. Quantitative evaluation of the damage to RC buildings caused by the 2023 southeast Turkey earthquake sequence. *Earthq. Spectra* **40**, 505–530 (2024).
19. USGS Geologic Hazards Science Center and Collaborators. The 2023 Kahramanmaraş, Turkey, Earthquake Sequence https://earthquake.usgs.gov/storymap/index-turkey2023.html (2024).
20. Görüm, T. et al. Preliminary documentation of coseismic ground failure triggered by the February 6, 2023 Türkiye earthquake sequence. *Eng. Geol.* **327**, 107315 (2023).
21. Bassal, P. et al. Liquefaction ground deformations and cascading coastal flood hazard in the 2023 Kahramanmaraş earthquake sequence. *Earthq. Spectra.* **40**, 87552930241247830 (2024).
22. Moug, D. M. et al. Liquefaction-induced ground and building interactions in İskenderun from the 2023 Kahramanmaraş earthquake sequence. *Earthq. Spectra* **40**, 913–938 (2024).
23. Yu, X. et al. Intelligent assessment of building damage of 2023 Turkey-Syria Earthquake by multiple remote sensing approaches. *npj Nat. Hazards* **1**, 3 (2024).
24. Robinson, C. et al. Turkey earthquake report. Tech. Rep. MSR-TR-2023-7, Microsoft https://www.microsoft.com/en-us/research/publication/turkey-earthquake-report/ (2023).
25. Voelker, B. et al. The EEFIT remote sensing reconnaissance mission for the February 2023 Turkey earthquakes. *IEEE Journal of Selected Topics in Applied Earth Observations and Remote Sensing* (2024).
26. Moehle, J. & Deierlein, G. G. A framework methodology for performance-based earthquake engineering. In *13th world conference on earthquake engineering*, vol. 679, 12 (WCEE Vancouver, 2004).
27. Porter, K. A. An overview of PEER's performance-based earthquake engineering methodology. In *Proceedings of ninth international conference on applications of statistics and probability in civil engineering*, 1–8 (Citeseer, 2003).
28. Chen, G., Yang, J., Liu, Y., Kitahara, T. & Beer, M. An energy-frequency parameter for earthquake ground motion intensity measure. *Earthq. Eng. Struct. Dyn.* **52**, 271–284 (2023).
29. Ilhan, O. et al. Local site effects at the selected stations affected by the February 6 2023 Türkiye Earthquake Sequences. *Soil Dyn. Earthq. Eng.* **178**, 108454 (2024).
30. Abdelmeguid, M. et al. Dynamics of episodic supershear in the 2023 M7. 8 Kahramanmaraş/Pazarcik earthquake, revealed by near-field records and computational modeling. *Commun. Earth Environ.* **4**, 456 (2023).
31. Akkar, S. & Bommer, J. J. Empirical equations for the prediction of PGA, PGV, and spectral accelerations in Europe, the Mediterranean region, and the Middle East. *Seismological Res. Lett.* **81**, 195–206 (2010).
32. Joyner, W. B. & Boore, D. M. Peak horizontal acceleration and velocity from strong-motion records including records from the 1979 Imperial Valley, California, Earthquake. *Bull. Seismological Soc. Am.* **71**, 2011–2038 (1981).
33. Chen, G., Liu, Y. & Beer, M. Effects of response spectrum of pulse-like ground motion on stochastic seismic response of tunnel. *Eng. Struct.* **289**, 116274 (2023).
34. Chen, G. et al. Seismic damage analysis due to near-fault multipulse ground motion. *Earthq. Eng. Struct. Dyn.* **52**, 5099–5116 (2023).
35. Sehhati, R., Rodriguez-Marek, A., ElGawady, M. & Cofer, W. F. Effects of near-fault ground motions and equivalent pulses on multi-story structures. *Eng. Struct.* **33**, 767–779 (2011).
36. Somerville, P. G., Smith, N. F., Graves, R. W. & Abrahamson, N. A. Modification of empirical strong ground motion attenuation relations to include the amplitude and duration effects of rupture directivity. *Seismological Res. Lett.* **68**, 199–222 (1997).
37. Federal Emergency Management Agency (FEMA). *Hazus Earthquake Model Technical Manual (Hazus 5.1)* https://www.fema.gov/sites/default/files/documents/fema_hazus-earthquake-model-technical-manual-5-1.pdf (2022).
38. Turkish Earthquake Code (TEC). Specification for buildings to be built in seismic zones. *Ministry of Public Works and Settlement, Government of the Republic of Turkey, Ankara, Turkey* (2007).
39. Turkish Building Earthquake Code (TBEC). Specification for buildings to be built in seismic zones. *Disaster and Emergency Management Presidency, Government of Republic of Turkey, Ankara, Turkey* (2018).
40. Alver, F., Kılıçarslan, Ö., Kuterdem, K., Türkoğlu, M. & Şentürk, M. D. Seismic Monitoring at the Turkish National Seismic Network (TNSN). *Summ. Bull. Int. Seismological Cent.* **53**, 41–58 (2019).
41. Gabriel, A.-A., Ulrich, T., Marchandon, M., Biemiller, J. & Rekoske, J. 3D Dynamic Rupture Modeling of the 6 February 2023, Kahramanmaraş, Turkey M w 7.8 and 7.7 Earthquake Doublet Using Early Observations. *Seismic Rec.* **3**, 342–356 (2023).
42. Işık, E. et al. Structural damages in masonry buildings in Adıyaman during the Kahramanmaraş (Turkiye) earthquakes (Mw 7.7 and Mw 7.6) on 06 February 2023. *Eng. Fail. Anal.* **151**, 107405 (2023).
43. Turan, A. I., Celik, A., Kumbasaroglu, A. & Yalciner, H. Assessment of reinforced concrete building damages following the Kahramanmaraş earthquakes in Malatya, Turkey (February 6, 2023). *Eng. Sci. Technol., Int. J.* **54**, 101718 (2024).
44. Özmen, A. et al. Seismic performance assessment of structures in Malatya Province after 6 February 2023 Turkey earthquake sequences. *Nat. Hazards* **141**, 1–34 (2024).
45. Disaster and Emergency Management Authority (AFAD). Turkish accelerometric database and analysis system https://tadas.afad.gov.tr/list-event (2024).
46. Turkish Statistical Institute (TURKSTAT). Survey on building and dwelling characteristics, 2021 https://data.tuik.gov.tr/Bulten/Index?p=Survey-on-Building-and-Dwelling-Characteristics-2021-45870&dil=2 (2021).
47. Humanitarian Data Exchange (HDX). Turkey - Population density (Nov. 2020). https://data.humdata.org/dataset/worldpop-population-density-for-turkey?utm_source=chatgpt.com.
48. Wackernagel, H. *Multivariate Geostatistics: An Introduction with Applications* (Springer Science & Business Media, 2003).
49. Chen, G., Liu, Y. & Beer, M. Identification of near-fault multi-pulse ground motion. *Appl. Math. Model.* **117**, 609–624 (2023).
50. Reitman, N. et al. Fault rupture mapping of the 6 February 2023 Kahramanmaraş, Türkiye, earthquake sequence from satellite data (ver. 1.1, February 2024). U.S. Geological Survey data release (2023). https://doi.org/10.5066/P985I7U2.
51. Global Shelter Cluster. Türkiye Earthquake 2023 - Damaged buildings https://sheltercluster.org/turkiye-earthquake-2023/pages/damaged-buildings (2023).
52. Emre, Ö. et al. Active fault database of turkey. *Bull. Earthq. Eng.* **16**, 3229–3275 (2018).

Acknowledgements
This work was financially supported by the Ministry of Education, Singapore, under its MOE AcRF Tier 3 Award no. MOE-MOET32021-0002 component D, "Integrating Volcano and Earthquake Science and Technology (InVEST)" to S.W., G.C., Z.M., and S.C.C. and by the National Natural Science Foundation of China (Grant No. U22A20596) and the Natural Science Foundation Innovation Group Project of Hubei Province, China (Grant No.2023AFA017) to Y.L. and G.C. All maps in this study were plotted using Generic Mapping Tools (GMT) version 6, while other figures and data were processed with MATLAB.

Author contributions
Conceptualization: G.C., S.W., Y.L. and S.C.C.; Methodology: G.C., J.Y., and S.W.; Investigation: G.C. and J.Y.; Visualization: G.C., J.Y., and Z.M.; Funding acquisition: S.W., Y.L., and S.C.C.; Project administration: S.W. and

Y.L.; Supervision: S.W., S.C.C., Y.L. and M.B.; Writing – original draft: G.C.; Writing – review and editing: All authors.

Competing interests

The authors declare no competing interests.

Additional information

Supplementary information The online version contains supplementary material available at https://doi.org/10.1038/s44304-025-00101-7.

Correspondence and requests for materials should be addressed to Yong Liu, Siau Chen Chian or Shengji Wei.